






Deep embrittlement and complete rupture of the lithosphere during the M_w 8.2 Tehuantepec earthquake

Diego Melgar ^{1*}, Angel Ruiz-Angulo ², Emmanuel Soliman Garcia³, Marina Manea ^{4,5}, Vlad. C. Manea ^{4,5}, Xiaohua Xu⁶, M. Teresa Ramirez-Herrera⁷, Jorge Zavala-Hidalgo⁸, Jianghui Geng⁹, Nestor Corona¹⁰, Xyoli Pérez-Campos¹¹, Enrique Cabral-Cano ¹¹ and Leonardo Ramirez-Guzmán¹²

Subduction zones, where two tectonic plates converge, are generally dominated by large thrust earthquakes. Nonetheless, normal faulting from extensional stresses can occur as well. Rare large events of this kind in the instrumental record have typically nucleated in and ruptured the top half of old and cold lithosphere that is in a state of extension driven by flexure from plate bending. Such earthquakes are limited to regions of the subducting slab cooler than 650 °C and can be highly tsunamigenic, producing tsunamis similar in amplitude to those observed during large megathrust events. Here, we show from analyses of regional geophysical observations that normal faulting during the moment magnitude M_w 8.2 Tehuantepec earthquake ruptured the entire Cocos slab beneath the megathrust region. We find that the faulting reactivated a bend-fault fabric and ruptured to a depth well below the predicted brittle-ductile transition for the Cocos slab, including regions where temperature is expected to exceed 1,000 °C. Our findings suggest that young oceanic lithosphere is brittle to greater depths than previously assumed and that rupture is facilitated by wholesale deviatoric tension in the subducted slab, possibly due to fluid infiltration. We conclude that lithosphere can sustain brittle behaviour and fail in an earthquake at greater temperatures and ages than previously considered.

Globally, since 1929, only seven shallow intraslab normal-faulting events with $M_w > 7.6$ have been recorded¹, all of these associated with bending stresses in the outer-rise region of the subduction zone. By contrast, 245 shallow thrust events have occurred in that time period². While comparatively rare, shallow normal-faulting events, often simply called outer-rise earthquakes, are of interest for hazards and for the geodynamics of subduction zones. The large majority of outer-rise events occur seaward of the trench³, and because they are shallow, they readily generate tsunamis. For example, the 1933 M_w 8.5 Sanriku earthquake generated a 20 m or greater tsunami¹ with wave amplitudes comparable to those observed during the large M_w 9.0 Tohoku-oki megathrust earthquake⁴. In terms of the geodynamics of subduction zones, the normal faults that host such events are key parts of the system^{3,5}. They are the product of flexure or bending, and previous observations shows they penetrate through the entire oceanic crust into the top few (~10) kilometres of the oceanic mantle⁶. Modelling shows that negative pressure gradients resulting from flexure can overcome lithostatic pressures and use these faults as pathways to facilitate seawater migration to mantle depths⁷. Hydration of the uppermost mantle has been confirmed by marine electromagnetic imaging⁸ showing high-conductivity regions associated with outer-rise abyssal hill fault structures. This process is essential for lithospheric mantle serpentinization, where water

reacts with both mafic and ultramafic rocks, forming hydrous serpentinite minerals. As the oceanic plate subducts, past the megathrust, dehydration reactions of these minerals occur and lead to high pore pressure, promoting failure in pre-existing bend-faulting fabric inherited from the outer rise⁹. This is the process of dehydration embrittlement³, considered to be the prevailing mechanism of intermediate-depth intraslab earthquakes.

In this context, the M_w 8.2 Tehuantepec earthquake (Fig. 1) ruptured in southern Mexico on 8 September 2017. The regional moment tensor solution from Mexico's National Seismological Service (Servicio Sismológico Nacional (SSN), <http://www.ssn.unam.mx>; Fig. 1) shows high-angle normal faulting (79° dip) striking at 310° with a hypocentre at 46 km depth, placing it still offshore but landward of the outer rise and trench underneath the continental shelf and subduction megathrust (Fig. 2). This portion of the megathrust is a mature seismic gap (the Tehuantepec seismic gap, Fig. 1a) that has not had a large thrust event since a $M_w \approx 8.6$ earthquake in 1787¹⁰. In this study, we present a robustly constrained model of the source process (Figs. 2 and 3) from joint inversion of strong motion, static global positioning system (GPS), high-rate GPS, tide gauges and ocean-bottom pressure sensors in the region (Fig. 3; Supplementary Fig. 1). We show that, unlike previous large normal-faulting events, which are restricted to thick, old plates and confined to the top half of the lithosphere cooler than 650 °C (ref. 3),

¹University of Oregon, Department of Earth Sciences, Eugene, OR, USA. ²Universidad Nacional Autónoma de México, Centro de Ciencias de la Atmósfera, Mexico City, Mexico. ³Kyoto University, Disaster Prevention Research Institute, Kyoto, Japan. ⁴Computational Geodynamics Laboratory, Centro de Geociencias, Universidad Nacional Autónoma de México, Campus Juriquilla, Querétaro, Mexico. ⁵Astronomical Institute of the Romanian Academy, Bucharest, Romania. ⁶University of California San Diego, Scripps Institution of Oceanography, La Jolla, CA, USA. ⁷Universidad Nacional Autónoma de México, Instituto de Geografía, Mexico City, Mexico. ⁸Universidad Nacional Autónoma de México, Servicio Mareográfico Nacional, Mexico City, Mexico. ⁹Wuhan University, GNSS Center, Wuhan, China. ¹⁰Colegio de Michoacán, Centro de Estudios en Geografía Humana, La Piedad, Mexico. ¹¹Universidad Nacional Autónoma de México, Instituto de Geofísica, Mexico City, Mexico. ¹²Universidad Nacional Autónoma de México, Instituto de Ingeniería, Mexico City, Mexico. *e-mail: dmelgarm@uoregon.edu

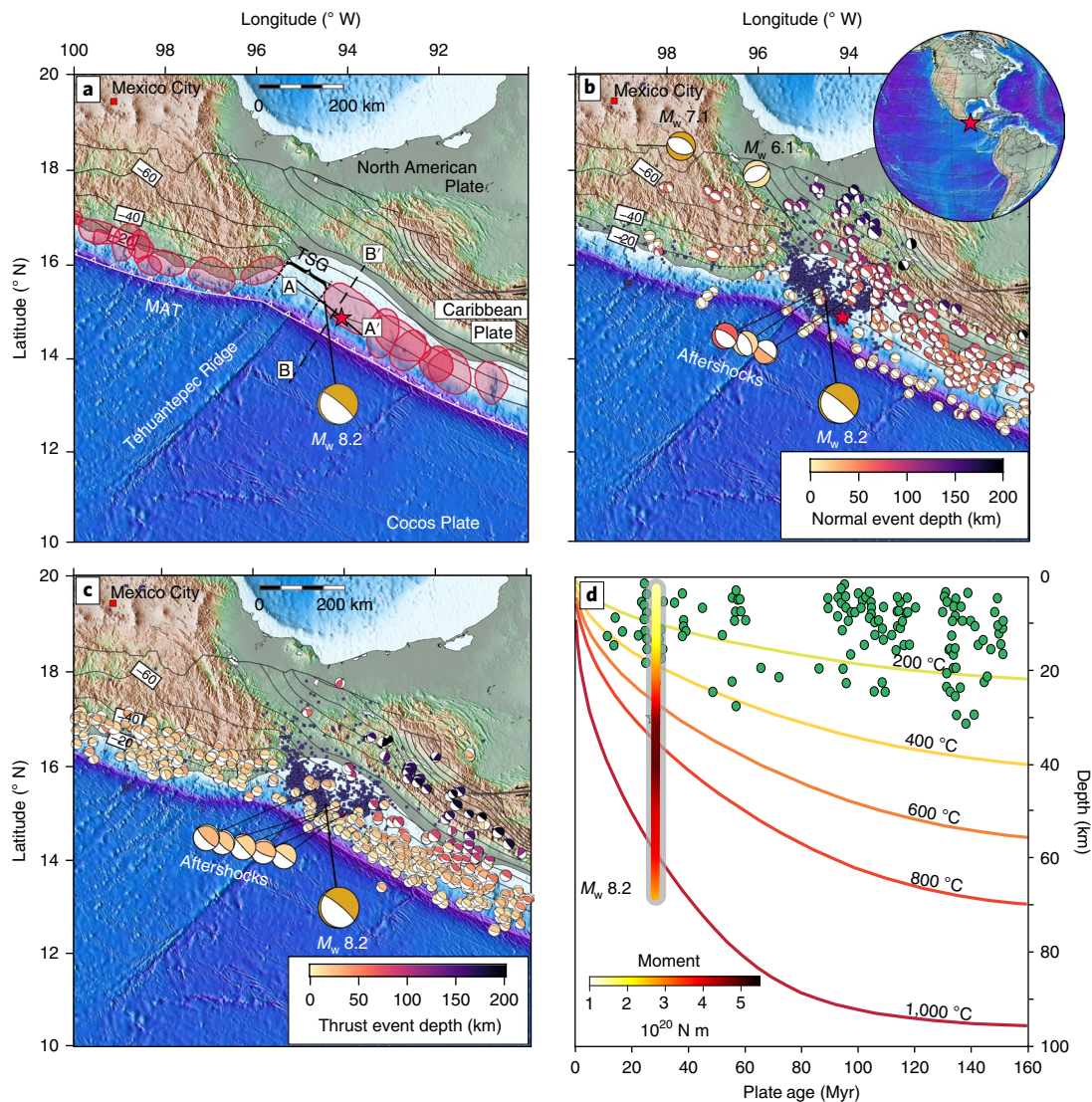


Fig. 1 | Regional tectonic context. **a**, Rupture areas of past megathrust events (red). Middle America Trench (MAT), slab depth contours (black) in kilometres²⁹. TSG is the Tehuantepec seismic gap. W-phase moment tensor from SSN. Cross sections AA' and BB' are shown in Figs 3b and 4b. **b**, Normal-faulting events before the mainshock. Offset beachballs are aftershocks. Dark blue squares are three weeks of aftershocks, and the red star is the mainshock. **c**, Same as **b** but for thrust events. **d**, Reference thermal model for the lithosphere and worldwide outer-rise normal-faulting events (green)¹. The mainshock moment (Fig. 2) is shown in the shaded grey area assuming a 25 Myr-old plate¹⁵. White is the event hypocentre. Depth is with respect to the top of the slab.

the Tehuantepec earthquake breaks a substantial portion, if not all, of the lithosphere (Fig. 4). We argue that this is possible because the entire lithosphere down dip is under wholesale deviatoric tension, even though flexure from bending predicts a combination of extension and compression. We observe a large shallow intraplate event slipping well past the predicted brittle–ductile transition into regions with temperatures as high as 1,100 °C, constrained by multiple geophysical datasets.

Source process of the Tehuantepec earthquake

For finite fault inversion, and to correctly interpret the geodynamic implications of the model, a robust hypocentral location is critical, since the assumed faulting surface is constrained to pass through it. Here, we use automatic and analyst revised P- and S-wave picks at regional broadband, strong-motion and short-period sites provided by SSN to locate the earthquake using a nonlinear inversion¹¹ and a regional velocity model¹². The hypocentre (Fig. 2) locates

28 km southwest (horizontal uncertainty is 1.6 km and vertical is 3 km), further offshore than the global teleseismic locations¹³. This is a well-known issue for earthquake locations in Mexico; a study of catalogue seismicity¹⁴ found that global velocity models introduce systematic northeastward biases that are on average 26 km. This is wholly consistent with our results. To further ascertain the reliability of our hypocentral location, we studied the differences between the regional and teleseismic locations for the largest aftershock (Fig. 2), the 23 September M_w 6.1 Ixtepec earthquake. This event is useful because it is shallow, and because it occurs onshore, we can study its deformation signal as measured by interferometric synthetic aperture radar (InSAR) and compare it with the hypocentral locations from regional and teleseismic data. We produced an unwrapped interferogram for this earthquake (Fig. 2; see Methods), which shows a clear deformation signal (~9 cm). With such a shallow earthquake, it is necessary for the hypocentre to be located inside the deformation zone. Indeed, our regional hypocentre

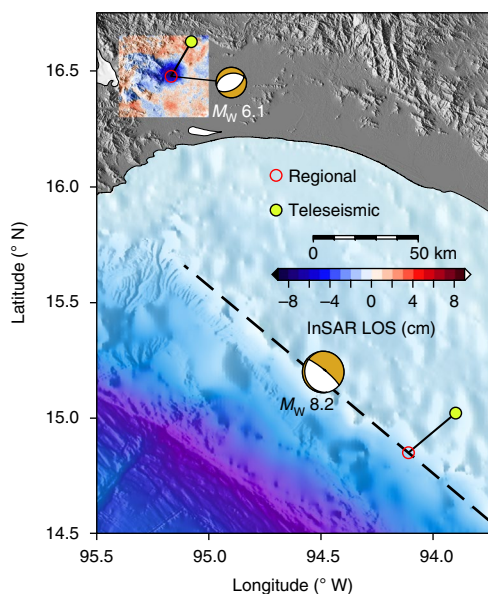


Fig. 2 | Hypocentral biases between regional and teleseismic locations.

Biases are shown for the M_w 8.2 mainshock and the largest (M_w 6.1) 23 September aftershock. We show the unwrapped Sentinel-1A interferogram for the M_w 6.1 aftershock spanning the acquisition dates 21 September to 3 October with a clear deformation signal. Note that the regional hypocentre falls well inside this deformation area, while the teleseismic hypocentre does not. The dashed line indicates the surface projection of the faulting surface used for kinematic inversion of the mainshock. InSAR LOS, InSAR line of sight.

locates at 10 km depth and inside this deformation zone, while the teleseismic location is 20 km northeast. This teleseismic hypocentre is well outside the deformation zone and biased in the same way as predicted by the analysis of catalogue seismicity¹⁴ and as seen for the mainshock. This is independent evidence that the regional locations are reliable and that the teleseismic locations have non-negligible biases.

Our finite fault model (Fig. 3; Supplementary Dataset 1) reveals fast rupture ($3.4\text{--}3.6\text{ km s}^{-1}$; Supplementary Fig. 2), consistent with the bulk of rupture lying in the lithospheric mantle, and slip larger than 3 m occurs from the hypocentre at 46 km updip to the intersection with the megathrust at 15 km and down to 80 km depth. The age of the slab in the earthquake region (25 Myr) is well constrained¹⁵, and its yield strength envelope (Fig. 4c) with the curvature at the hypocentral position (Fig. 4a) shows that yielding related to bending stresses is possible in only the top ~ 36 km of the slab. In this region, only the first ~ 18 km can yield under tension, while the next 18 km can yield under compression. A comparison with a thermal model for the region¹⁶ shows rupture nucleates at the $\sim 700^\circ\text{C}$ geotherm and the bulk of moment release occurs downdip, extending up to $1,100^\circ\text{C}$. The multi-data inversion is key to reliably interpreting this unique seismic event. Static GPS and tsunami data from tide gauges and one DART (Deep-ocean Assessment and Reporting of Tsunamis) buoy that measures ocean-bottom pressure, provide strong constraints on total moment (M_w 8.2). Meanwhile, the depth extent of rupture is well resolved by 55 high-rate GPS displacement and strong-motion velocity waveforms; these data are sensitive to the timing and locus of slip¹⁷. Fortunately, the geography of the Gulf of Tehuantepec and the distribution of geophysical stations in southern Mexico provide an excellent azimuthal coverage

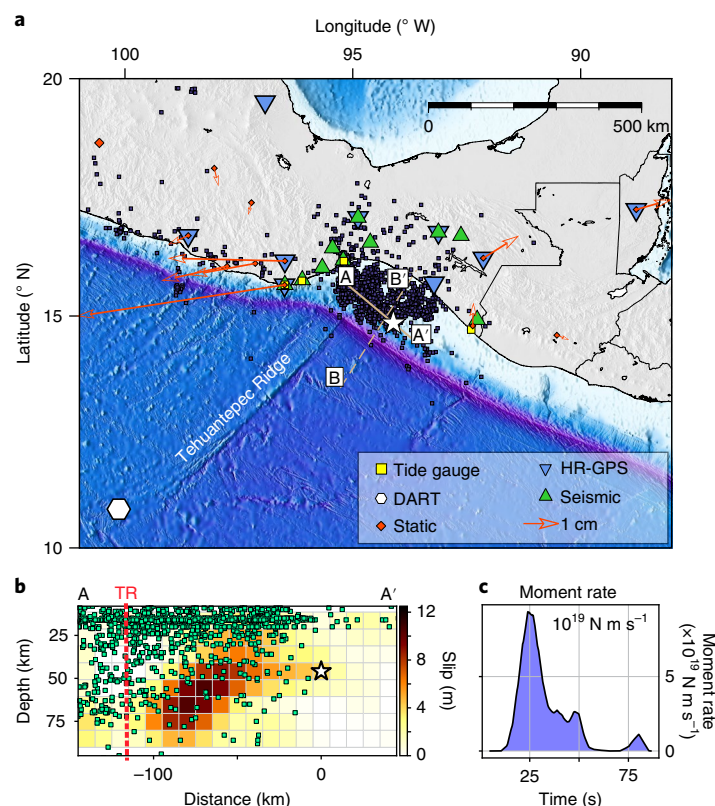


Fig. 3 | Results of the kinematic slip inversion. a, Data used in the inversion. Shown are strong motion, tide gauge, ocean-bottom pressure (DART), static GPS (orange arrows) and high-rate GPS (HR-GPS) sites. Dark blue squares are one month of aftershocks, and the white star is the hypocentre. **b**, Slip inversion from joint inversion of all data. Green squares are the aftershocks within 10 km of profile AA'. The orange line labelled TR is the intersection of the subvertical fault plane with the projection of the Tehuantepec Ridge. **c**, Source time function for the slip inversion.

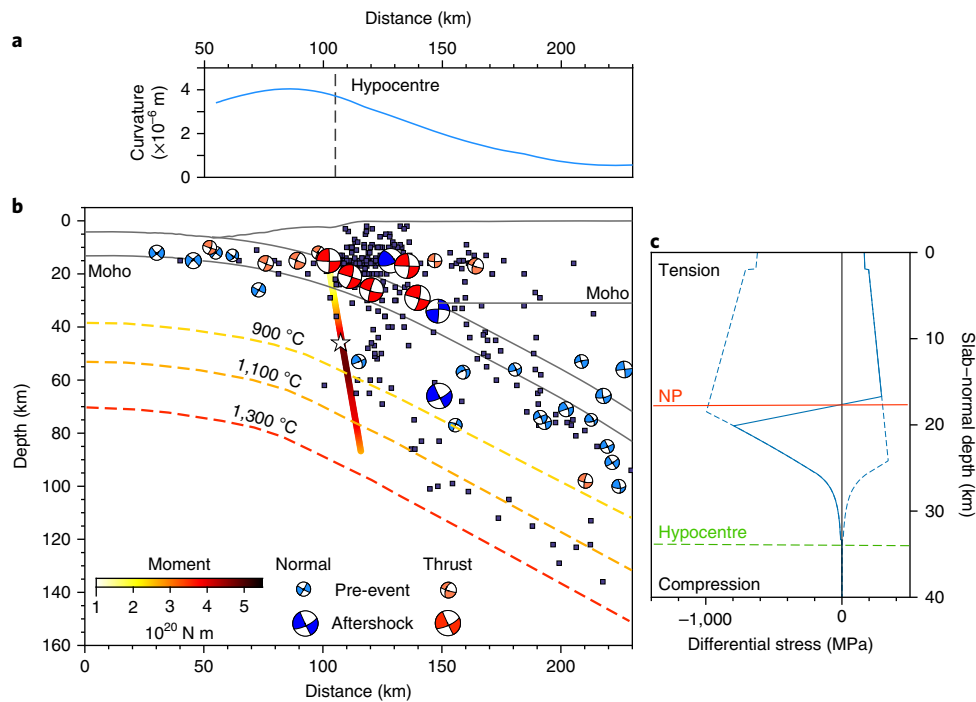


Fig. 4 | Deep embrittlement during the rupture. **a, b**, Profile BB' showing curvature of the subducted slab (**a**) and slab geometry²⁹, oceanic crustal thickness from global tomography³⁶ and continental Moho receiver functions³⁷, the dashed line indicates the hypocentre position. (**b**). Modelled geotherms¹⁶ are indicated as dashed lines. Moment tensors are for the pre-event seismicity and for events $M_w > 5$ aftershocks in the first month. Strike-averaged moment from the inversion (Fig. 3) is plotted. The white star is the event hypocentre. Dark blue squares are aftershock locations. Black lines indicate the oceanic and continental crusts. **c**, Yield strength envelope (blue solid and dashed lines) for a 25 Myr-old slab. NP indicates the neutral plane above which there is flexural tension and below which is compression. The green dashed line is the slab-normal depth of the hypocentre.

of the rupture. This deep extent of rupture is consistent with global point-source centroid moment tensor seismic models. The centroid of moment release of our slip model (Fig. 3) is at 54 km, in line with 47 km for the United States Geological Survey model and 50 km for the Global Centroid Moment Tensor model.

Reliability of the inferred deep slip

Reliability of the deep extent of rupture in our model is a critical issue. We conducted a formal resolution analysis of the slip inversion (Supplementary Fig. 3). Individually, some datasets can allow depth resolution (for example, GPS static offsets); however, our checkerboard analyses show that the combined multi-data inversion has no depth-dependent biases and can recover deep slip reliably. In our inversion geometry, slip can extend to 90 km depths. However, to further buttress this finding, we performed three further trial inversions, restricting the deepest possible slip to 60 km, 70 km and 80 km and using the same data weight and regularization as in our preferred inversion (Supplementary Fig. 4). We find that the best fits to the combined data are for the fault model that allows slip down to 90 km (Supplementary Figs. 5–8).

A previous finite fault inversion from joint inversion of teleseismic and DART buoy data by Ye et al.¹⁸ show similar depths of slip (30–70 km). However, they assume the biased teleseismic hypocentre (Fig. 2), which is further inland. This led them to conclude that, when assuming a 30 km thickness of the brittle part of the plate (the depth to the 600 °C isotherm), then the slip penetrated at most 10 km into regions hotter than 600 °C. Thus, the Ye et al.¹⁸ model ruptures through only the brittle part of the lithosphere and does not penetrate into the bottom portion of the lithosphere. Conversely, our model relies on regional geophysical data that have improved depth sensitivity compared with teleseismic data, and furthermore, we use

a better constrained hypocentre. Additionally, pre-event seismicity as well as a large number of aftershocks also extend into the 1,100 °C geotherm area. Considering all of these factors, and that the base of the lithosphere is at ~1,150 °C (ref.¹⁹), this earthquake must have ruptured all or most of the entire oceanic lithosphere.

Deep embrittlement in the Cocos slab

A calculation of the curvature of the slab (Fig. 4a) shows that the event nucleates away from the point of maximum curvature and ruptures in a region where unbending of the slab is currently occurring. The strike of the earthquake (310°) is in close agreement with the strike of the incoming plate fabric fault scarps (320°) (ref.⁹) and of outer-rise normal-faulting events in the region (315°; Fig. 1b; Supplementary Fig. 9). Also, given the substantial length and width of the Tehuantepec earthquake (~150 km × 70 km), we consider that the earthquake ruptured pre-existing planes of weakness inherited from the outer-rise region. The kinematic slip model of the earthquake challenges current structural models of subduction kinematics; there is normal-faulting (extensional) rupture throughout the entire lithosphere at a point where curvature is high and through portions that should be in flexural compression, and furthermore, rupture spreads well past the 650 °C geotherm (Figs. 1d and 4) into regions where global surveys find that no normal or thrust-faulting intraslab outer-rise-associated seismicity has ever been observed³. At the nucleation depth in the bottom half of the oceanic lithosphere, the slab appears to be in tension, contrary to what is predicted from mere flexure (Fig. 4c). Previous analyses of worldwide intraslab events¹ have shown that deepening of the tensional regime can be explained by a combination of increased slab pull, low coupling along the megathrust and no slab ponding at the 660 km discontinuity, and there is evidence for this in the Tehuantepec region.

Seismic tomography²⁰ shows a detached slab at ~300 km depth and no ponding of the slab at the 660 km discontinuity (a source of intraslab compression). Overwhelmingly normal-faulting intermediate-depth events downdip of the mainshock region (Fig. 1b,c) further confirm slab pull is strong here. Extensional stresses are usually easily transmitted through the lithosphere updip³, but strong coupling at the megathrust can impede this. This is unlikely to occur at the Tehuantepec event source region due to the existence of the long-lived Tehuantepec seismic gap. Limited-resolution onshore geodetic observations suggest moderate to low coupling along the megathrust²¹. Combining these observations, we conclude that, in spite of slab curvature being high (Fig. 3a), the entire lithosphere is under wholesale deviatoric tension, explaining the unusual location of a normal-faulting mechanism in areas expected to be in compression and extending to the base of the lithosphere. However, deep slip down to the 1,100 °C geotherm requires a substantial deviation from the reference thermal model, suggesting very deep injection of fluids from above and cooling of the fault. This indicates fluid penetration much deeper than any of the modelling or observations have suggested before^{6–8}. Alternatively, a water-independent process that increases the range of possible temperatures for earthquake slip up to 850 °C could induce shear heating instabilities on localized shear zones²².

Thus, combined seismological and geodetic observations of the 2017 M_w 8.2 Tehuantepec, Mexico, earthquake reveal that almost the entire oceanic lithosphere, including the mantle and crust, ruptured in a single large intraslab normal-fault earthquake. It is possible that the 1931 normal-faulting M_w 8.0 Oaxaca earthquake, just east of the Tehuantepec Ridge, similarly broke the entire lithosphere²³ and that both events are part of an ongoing larger-scale breakdown of the slab; however, limited historical seismograms make that determination difficult. Here, we have shown conclusively, with a wide diversity of geophysical observations, that under the right conditions, large earthquakes can nucleate in and rupture through the entire oceanic plate, even for young subduction zones. The likely causal chain for the M_w 8.2 Tehuantepec intraslab event is: (1) a large normal fault, dipping at 45° or greater, is formed from reactivated abyssal hill fabric at the outer rise, and this fault does not extend past the traditional flexural neutral plane; (2) as the fault enters into subduction and approaches the megathrust region, it steepens in dip, and encountering a slab increasingly in tension, it grows deeper into the slab; finally, (3) unbending and wholesale deviatoric tension from strong slab pull forces activates the normal fault, and deep fluid injection or shear heating trigger faulting through most of the lithosphere, even though the surrounding slab is predicted to be in a creep regime (Supplementary Fig. 10).

Early studies suggested that the 1933 M_w 8.6 Sanriku normal-faulting event²⁵ similarly ruptured the entire lithosphere. However, recent reappraisals with modern techniques of the tsunami and seismic data for that event¹ find that it is more likely it ruptured just the upper half undergoing flexural extension and that the large seismogenic thickness of the old and cold slab in northern Japan allowed such a high-magnitude event. Additionally, previously recorded large flexure, shallow normal-faulting events proximal to the trench (like the Sanriku earthquake) are observed for lithosphere older than 100 Myr only^{1,3}. For the young Tehuantepec slab (25 Myr), the strength envelope for plate flexure predicts no more than 18 km of available seismogenic thickness (Fig. 4c), suggesting that only modest magnitude should be expected. Both of these conditions argue that the large shallow intraplate normal-faulting events in the Tehuantepec area are fundamentally different from their counterparts in older and colder slabs, which are mostly driven by flexural stresses. Finally, a critical unanswered question for hazards is how far offshore deviatoric tension can allow anomalously large normal faults to extend to deeper depths and into areas expected to be in compression. The 8 September M_w 8.2 mainshock produced only

a modest (~3 m) tsunami²⁴; however, if similar events can occur closer to the trench, or even outboard of it, then catastrophic tsunami impacts akin to those seen in the 1933 Sanriku event^{1,25} should be considered possible in hazard maps of the Tehuantepec region.

Online content

Any methods, additional references, Nature Research reporting summaries, source data, statements of data availability and associated accession codes are available at <https://doi.org/10.1038/s41561-018-0229-y>.

Received: 25 January 2018; Accepted: 17 August 2018;

Published online: 01 October 2018

References

- Okal, E. A., Kirby, S. H. & Kalligeris, N. The Showa Sanriku earthquake of 1933 March 2: a global seismological reassessment. *Geophys. J. Int.* **206**, 1492–1514 (2016).
- Storchak, D. A. et al. Public release of the ISC–GEM Global Instrumental Earthquake Catalogue (1900–2009). *Seism. Res. Lett.* **84**, 810–815 (2013).
- Mori, N. et al. Nationwide post event survey and analysis of the 2011 Tohoku earthquake tsunami. *Coastal Eng. J.* **54**, 1250001 (2012).
- Craig, T. J., Copley, A. & Jackson, J. A reassessment of outer-rise seismicity and its implications for the mechanics of oceanic lithosphere. *Geophys. J. Int.* **197**, 63–89 (2014).
- Peacock, S. M. Are the lower planes of double seismic zones caused by serpentine dehydration in subducting oceanic mantle? *Geology* **29**, 299–302 (2001).
- Ranero, C. R., Morgan, J. P., McIntosh, K. & Reichert, C. Bending-related faulting and mantle serpentinization at the Middle America trench. *Nature* **425**, 367–373 (2003).
- Faccenda, M., Gerya, T. V. & Burlini, L. Deep slab hydration induced by bending-related variations in tectonic pressure. *Nat. Geosci.* **2**, 790–793 (2009).
- Naif, S., Key, K., Constable, S. & Evans, R. L. Water-rich bending faults at the Middle America trench. *Geochem. Geophys. Geosyst.* **16**, 2582–2597 (2015).
- Ranero, C. R., Villaseñor, A., Phipps Morgan, J. & Weinrebe, W. Relationship between bend-faulting at trenches and intermediate-depth seismicity. *Geochem. Geophys. Geosyst.* **6**, Q12002 (2005).
- Suárez, G. & Albin, P. Evidence for great tsunamigenic earthquakes (M 8.6) along the Mexican subduction zone. *Bull. Seism. Soc. Am.* **99**, 892–896 (2009).
- Herrmann, R. B. Computer programs in seismology: an evolving tool for instruction and research. *Seism. Res. Lett.* **84**, 1081–1088 (2013).
- Hernandez, B. et al. Rupture history of September 30, 1999 intraplate earthquake of Oaxaca, Mexico (M_w = 7.5) from inversion of strong-motion data. *Geophys. Res. Lett.* **28**, 363–366 (2001).
- M* 8.2—101 km SSW of Tres Picos, Mexico (United States Geological Survey, accessed 23 January 2018); <https://earthquake.usgs.gov/earthquakes/eventpage/us2000ahv0>
- Hjörleifsdóttir, V., Singh, S. K. & Husker, A. Differences in epicentral location of Mexican earthquakes between local and global catalogs: an update. *Geofis. Int.* **55**, 79–93 (2016).
- Müller, R. D., Sdrolias, M., Gaina, C. & Roest, W. R. Age, spreading rates and spreading symmetry of the world's oceanic crust. *Geochem. Geophys. Geosyst.* **9**, Q04006 (2008).
- Manea, V. C. & Manea, M. in *Volcanic Hazards in Central America* Vol. 412 (eds Rose, W. I. et al.) 27–38 (GSA Special Papers, Geological Society of America, 2006).
- Melgar, D. et al. Slip segmentation and slow rupture to the trench during the 2015, M_w 8.3 Illapel, Chile earthquake. *Geophys. Res. Lett.* **43**, 961–966 (2016).
- Ye, L., Lay, T., Bai, Y., Cheung, K. F. & Kanamori, H. The 2017 M_w 8.2 Chiapas, Mexico, earthquake: energetic slab detachment. *Geophys. Res. Lett.* **44**, 11824–11832 (2017).
- Hillis, R. R. & Müller, R. D. in *Evolution and Dynamics of the Australian Plate* Vol. 372 (eds Hillis, R. R. & Müller, R. D.) 1–5 (GSA Special Papers, Geological Society of America, 2003).
- Rogers, R. D., Káráson, H. & van der Hilst, R. D. Epeirogenic uplift above a detached slab in northern Central America. *Geology* **30**, 1031–1034 (2002).
- Franco, A. et al. Fault kinematics in northern Central America and coupling along the subduction interface of the Cocos Plate, from GPS data in Chiapas (Mexico), Guatemala and El Salvador. *Geophys. J. Int.* **189**, 1223–1236 (2012).
- Kelemen, P. B. & Hirth, G. A periodic shear-heating mechanism for intermediate-depth earthquakes in the mantle. *Nature* **446**, 787–790 (2007).

23. Singh, S. K., Suárez, G. & Domínguez, T. The Oaxaca, Mexico, earthquake of 1931: lithospheric normal faulting in the subducted Cocos Plate. *Nature* **317**, 56–58 (1985).
24. Ramírez-Herrera, M. T., Corona, N., Ruiz-Angulo, A., Melgar, D. & Zavala-Hidalgo, J. The 8 September 2017 tsunami triggered by the M_w 8.2 intraplate earthquake, Chiapas, Mexico. *Pure Appl. Geophys.* **175**, 25–34 (2018).
25. Kanamori, H. Seismological evidence for a lithospheric normal faulting—the Sanriku earthquake of 1933. *Phys. Earth Planet. Int.* **4**, 289–300 (1971).
29. Hayes, G. P., Wald, D. J. & Johnson, R. L. Slab1.0: a three-dimensional model of global subduction zone geometries. *J. Geophys. Res.* **117**, B01302 (2012).
36. Pasyanos, M. E., Masters, T. G., Lasko, G. & Ma, Z. LITHO1.0: an updated crust and lithospheric model of the Earth. *J. Geophys. Res.* **119**, 2153–2173 (2014).
37. Melgar, D. & Pérez-Campos, X. Imaging the Moho and subducted oceanic crust at the Isthmus of Tehuantepec, Mexico, from receiver functions. *Pure Appl. Geophys.* **168**, 1449–1460 (2011).

Acknowledgements

We thank D. Toomey, R. Burgmann and D. Sandwell for discussions. Strong-motion data used in this work were provided by Servicio Sismológico Nacional (SSN, Mexican National Seismological Service), and Unidad de Instrumentación Sísmica (UIS) at the Instituto de Ingeniería (II), Universidad Nacional Autónoma de México (UNAM, National Autonomous University of Mexico). We thank their personnel for station maintenance, data acquisition and distribution. This material is partly based on data provided by the Transboundary, Land and Atmosphere Long-term Observational and Collaborative Network (TLALOCNet) operated by UNAVCO and the Servicio de Geodesia Satelital from Instituto de Geofísica-UNAM and supported by NSF grant EAR-1338091, CONACyT project 253760 and UNAM-PAPIIT projects IN104213 and IN109315-3. L. Salazar-Tlaczani at Servicio de Geodesia Satelital-UNAM provided invaluable support for the TLALOCNet field operations and stations maintenance. We are indebted to the staff and technicians of the Servicio Mareográfico Nacional who operate the tide gauge network. Some numerical computations were performed at the

National Laboratory for Advanced Scientific Visualization at UNAM (LAVIS), and this work received support from LAVIS software engineers L. A. Aguilar Bautista, A. de León Cuevas and C. S. Flores Bautista. This research project was partially supported by the Japanese government through the programme Science and Technology Research Partnership for Sustainable Development (SATREPS) via the Japan International Cooperation Agency (JICA) and the Japan Science and Technology Agency (JST) with Grant Number 15543611. This work was also supported by a grant from the Romanian Ministry of National Education and Scientific Research, RDI Program for Space Technology and Advanced Research—STAR, project ID 513.

Author contributions

D.M. and A.R.-A. conceived and carried out the study. D.M. performed the slip inversion analysis. A.R.-A. analysed the sea-level data. E.S.G. performed the curvature and flexure calculations. M.M. and V.C.M. carried out the thermal modelling. D.M., A.R.-A., E.S.G., M.M. and V.C.M. created the figures and wrote the paper. X.X. carried out the InSAR analysis. M.T.R.-H., J.Z.-H. and N.C. provided and analysed the tsunami data. J.G. processed the high-rate GPS data. X.P.-C., E.C.-C. and L.R.-G. maintain and operate the seismic and geodetic networks. All authors discussed the results and revised the manuscript and figures.

Competing interests

The authors declare no competing interests.

Additional information

Supplementary information is available for this paper at <https://doi.org/10.1038/s41561-018-0229-y>.

Reprints and permissions information is available at www.nature.com/reprints.

Correspondence and requests for materials should be addressed to D.M.

Publisher's note: Springer Nature remains neutral with regard to jurisdictional claims in published maps and institutional affiliations.

Methods

Static and high-rate GPS data. We processed 1 Hz and 5 Hz continuous GPS data from the TLALOCNet (Transboundary, Land and Atmosphere Long-term Observational and Collaborative Network) GPS network for the day of the mainshock. Final GPS satellite orbits, Earth rotation parameters and 0.2 Hz GPS satellite clocks from the Center for Orbit Determination in Europe ([ftp://ftp.unibe.ch/aiub/CODE/2017/](http://ftp.unibe.ch/aiub/CODE/2017/)) were fixed to estimate 1 Hz satellite clocks and 30 s fractional-cycle biases and fractional-cycle biases with reference stations located over 1,000 km from the epicentral zone. We then fixed the orbits, clocks and Earth rotation parameters to enable precise point positioning with ambiguity resolution, to estimate epoch-wise positions along with zenith troposphere delay parameters, receiver clocks and integer-cycle phase ambiguities for all high-rate stations. All position estimates are with respect to the International Terrestrial Reference Frame (ITRF2008) positions and are not contaminated by any displaced reference stations. No constraints between epochs are applied to the positions, while zenith troposphere delays are estimated as random-walk parameters with a process noise of $(1 \text{ mm s}^{-1})^{12}$. All eligible ambiguities were resolved successfully. Solid Earth tide, ocean tide loading and pole tide are applied, and antenna phase centre variations are also corrected. According to the scatter of 10 min of pre-event positions, the position precision (one sigma) is about 5 mm for the horizontal and 10 mm for the vertical components for all stations. The GPS waveforms are low-pass filtered to 0.5 Hz before inversion. Static GPS data are from the 24-hour rapid solution provided by the Nevada Geodetic Laboratory (<http://geodesy.unr.edu/>).

Data preprocessing. We removed tides for 6 days of high sample rate (60 s) tide gauge data (2 days before and 4 days after the event) and 24 hours of DART buoy data (the day of the event). DART buoy data have irregularly spaced samples, so they were resampled to a 60 s sample rate. Tide gauge and DART buoy data were bandpass filtered between periods of 10 min and 2 hours before inversion. The pre-event mean was removed from the strong-motion data and bandpass filtered between 0.02 Hz and 0.3 Hz to remove baseline offsets. We then integrated to velocity and resampled from 100 Hz or 200 Hz to 4 Hz. The high-rate GPS data were first low-pass filtered to 0.3 Hz and resampled from 1 Hz or 5 Hz to 4 Hz for inversion.

Finite fault inversion. We use a multi-time window code for slip inversion²⁶. We used the main nodal plane from the SSN W-phase moment tensor (Fig. 1) solution with a strike of 309° and dip of 79° to define the faulting surface. This nodal plane was chosen after trying the inversion on both nodal planes. The shallow dipping nodal plane does not fit the data as well. We further constrain the slip surface to go through the hypocentre (94.459216°W , 15.051190°N , 45.9 km). The assumed fault was discretized into $152 \times 10 \text{ km} \times 10 \text{ km}$ subfaults. Green's functions for every data type (GPS, strong motion and tsunami) were computed for each subfault/station pair. Elastostatic and dynamic displacement Green's functions at 1 Hz and 5 Hz GPS sample rates (depending on the station) were computed using the frequency wavenumber integration technique and resampled to 4 Hz for inversion. All the Green's functions data are filtered in the same pass bands as the input data. Static Green's functions are calculated using the same method. We assume a layered regional velocity model for the Oaxaca region¹². For the Tsunami Green's functions at the tide gauge and DART buoy locations, we use GeoClaw²⁷, a shallow-water equation-solving code. We assume 1 m of slip at each subfault and calculate seafloor deformation using the same layered Earth model. The seafloor deformation is then the initial condition for a tsunami excitation, resulting in a Green's function at each site for each subfault. Bathymetry for the calculation is 450 m pixels from the Shuttle Radar Topography Mission 15_PLUS dataset²⁸. Joint inversion of the strong-motion, GPS static offsets, high-rate waveforms, tide gauge and DART buoy data was carried out using the multi-time window method with three-knot splines (isosceles triangles) as basis functions¹⁷. To model the complexity of the subfault source time functions, we allowed slip on nine 50% overlapping triangles with 2 s rise times. Spatial regularization was achieved through Laplacian smoothing, penalizing rough slip distributions; constraints were placed on the L_2 norm of the model parameter vector. Temporal smoothing on the time windows was achieved with a simple first-order forward finite difference stencil²⁶. The four data types (static GPS, high-rate GPS, strong motion and tsunami) were weighted equally by dividing each dataset by the norm of the vector containing the observations. Care was taken to calibrate the maximum rupture speed in the inversion. It was constrained through trial and error (Supplementary Fig. 2); 50 inversions with varying levels of regularization were run at maximum rupture speeds between 2.6 km s^{-1} and 4.4 km s^{-1} in 0.1 km s^{-1} bins. This is a total of 700 separate inversions. At each regularization level, the fits to each dataset are disaggregated and averaged across regularization levels. The mean fits as a function of rupture speed are plotted in Supplementary Fig. 2. We conclude that all the data are best explained by a maximum rupture speed of $3.4\text{--}3.6 \text{ km s}^{-1}$. To study spatial resolution, we conducted a standard checkerboard test. A synthetic checkerboard slip distribution (Supplementary Fig. 3) was created, and all the data for the same stations used in the inversion were simulated. The data were contaminated with noise and inverted using the same regularization parameter from the final joint inversions. A total of five inversions were carried out, one for each individual dataset and one for the joint inversion, and we

retained the same weights as used in the final inversion. Results of the test are in Supplementary Fig. 4 and show the relative contributions of each data type, with the joint inversion having the best recovery of the input pattern, with no substantial blurring of deep slip.

Slab curvature calculation. The extrinsic curvature of the slab interface is one way of quantifying how flat or warped the oceanic lithosphere becomes as it subducts into the upper mantle. In this work, we use it mainly as a proxy for the curvature of a thin plate along a principal stress direction. We refer to the Slab1.0 model²⁹ for the depth to the top of the subducting slab, which is based on fitting an optimal surface to earthquake hypocentre locations. We compute the local derivative of the dip angle with respect to a tangent segment³⁰. When the slab interface is smoothly varying along strike, this local dip gradient approximates the second derivative of the plate deflection along a profile aligned with the downdip direction. We make a further assumption that for the case of the Cocos Plate in the vicinity of the earthquake slip region, the value of this along-dip gradient is also a suitable enough approximation for the plate curvature in the direction of slab bending.

Strength envelope calculation. We estimate the difference between downdip and slab-normal stresses in the subducting oceanic lithosphere using a simple layered rheology. In a thin plate behaving elastically, the material above the mid- or neutral plane is in a tensional regime, whereas the lower half of the plate is in compression. The magnitude of the elastic bending stress at a given depth is directly proportional to the plate curvature and the distance from the neutral plane. However, Earth materials such as the oceanic lithosphere can sustain differential stresses only up to a limit called the yield strength. Yielding can take place as a result of either brittle failure or ductile creep. The brittle strength is determined from the frictional properties of pre-existing fractures and linearly increases with normal stress, while ductile creep is temperature dependent and is typically related to the strain rate in a nonlinear way. The empirical relations for calculating these yield criteria are constrained using laboratory experiments on rock samples. A yield strength envelope can then be constructed by selecting the criterion that gives the lower magnitude of yield strength. Following this approach³¹, the bending stresses become limited by brittle faulting in the shallow lithosphere and inhibited by ductile flow at greater depths. For the material constituting the subducted oceanic lithosphere, the transition between these types of mechanical behaviour is probably not as drastic as portrayed by the yield strength envelope. However, this idealized representation can provide qualitative insights into the effects of bending stresses on slab deformation. Some additional assumptions are made. When high pore fluid pressures are present, the normal stress on the pre-existing faults is reduced. The upper crust in the slab is assumed to have a higher pore fluid ratio than the lower crust due to densification. Thus, even if creep mechanisms are activated by reheating at the slab interface or cataclastic flow occurs, the brittle failure strength remains the minimum yield value.

InSAR processing. We used InSAR data acquired by the Sentinel-1 satellites operated by the European Space Agency. We processed an interferometric pair from the Sentinel-1 satellites descending track 172 acquired between 19 and 25 September. These dates span the occurrence of the largest aftershock, the M_w 6.1 Ixtepec earthquake on 23 September. This pair has the shortest possible temporal baseline available at the time of 6 days. The data were processed with pure geometric coregistration³² using open-source software GMTSAR³³. The postprocessing was done using the Generic Mapping Tools³⁴. We applied a 400 m low-pass filter to suppress phase noise and decorrelation from the dense vegetation over this region. Interferograms from different subswaths were stitched together and then unwrapped using the statistical-cost network-flow algorithm for phase unwrapping (SNAPHU³⁵). After unwrapping, a linear ramp was removed using data far away from the area of coseismic deformation to correct for possible atmospheric effect. We use the sign convention to indicate positive motion towards the satellite and negative motion away from the satellite.

Code availability. The slip inversion code (MudPy) is freely available on GitHub (<https://github.com/dmelgarm/MudPy>). The InSAR processing code (GMTSAR) is also freely available (<http://topex.ucsd.edu/gmtsar/>). Analysis and plotting scripts are available upon request from the corresponding author.

Data availability

Strong-motion data are available from the Strong Ground Motion Database System (<http://aplicaciones.iingen.unam.mx/AcelerogramasRSM/>) and by email request to SSNdata@sismologico.unam.mx. Receiver Independent Exchange Format files with the raw GPS observations from the TLALOCNet archive are open and freely available at <http://tlalocnet.udg.mx> as well as at the UNAVCO archive <https://www.unavco.org/data/data.html>. University of Nevada, Reno static offset solutions are available at http://geodesy.unr.edu/news_items/Offsets_Pijijiapan_rapid24hr.txt. Tide gauge data are provided by Servicio Mareográfico Nacional from Universidad Nacional Autónoma de México and are available at <http://www.mareografico.unam.mx/> and at <http://www.ioc-sealevelmonitoring.org/>. DART buoy data can be obtained from <https://www.ndbc.noaa.gov/dart.shtml>.

References

26. Melgar, D. & Bock, Y. Kinematic earthquake source inversion and tsunami runup prediction with regional geophysical data. *J. Geophys. Res. Solid Earth* **120**, 3324–3349 (2015).
27. LeVeque, R. J., George, D. L. & Berger, M. J. Tsunami modelling with adaptively refined finite volume methods. *Acta Numer.* **20**, 211–289 (2011).
28. Becker, J. J. et al. Global bathymetry and elevation data at 30 arc seconds resolution: SRTM30_PLUS. *Mar. Geod.* **32**, 355–371 (2009).
30. Bletery, Q. et al. Mega-earthquakes rupture flat megathrusts. *Science* **354**, 1027–1031 (2016).
31. Wang, K., Wada, I. & Ishikawa, Y. Stresses in the subducting slab beneath southwest Japan and relation with plate geometry, tectonic forces, slab dehydration, and damaging earthquakes. *J. Geophys. Res.* **109**, B08304 (2004).
32. Xu, X., Sandwell, D. T., Tymofeyeva, E., González-Ortega, A. & Tong, X. Tectonic and anthropogenic deformation at the Cerro Prieto geothermal step-over revealed by Sentinel-1A InSAR. *IEEE Trans. Geosci. Remote Sens.* **55**, 5284–5292 (2017).
33. Sandwell, D., Mellors, R., Tong, X., Wei, M. & Wessel, P. Open radar interferometry software for mapping surface deformation. *Eos Trans. AGU* **92**, 234–234 (2011).
34. Wessel, P., Smith, W. H., Scharroo, R., Luis, J. & Wobbe, F. Generic Mapping Tools: improved version released. *Eos Trans. AGU* **94**, 409–410 (2013).
35. Chen, C. W. & Zebker, H. A. Network approaches to two-dimensional phase unwrapping: intractability and two new algorithms. *J. Opt. Soc. Am. A* **17-3**, 401–414 (2000).